remote sensing

IMPACT FACTOR 5.0

CITESCORE 7.9

Article

# The Bureya Landslide Recent Evolution According to Spaceborne SAR Interferometry Data

Alexander Zakharov and Liudmila Zakharova

Special Issue
Landslide and Volcanoes: Recent Advances in Process Understanding
Edited by
Dr. Anja Dufresne and Prof. Dr. Nicole Richter

MDPI

https://doi.org/10.3390/rs14205218

*remote sensing*

MDPI

*Article*

# The Bureya Landslide Recent Evolution According to Spaceborne SAR Interferometry Data

**Alexander Zakharov and Liudmila Zakharova ***

Kotel'nikov Institute of Radioengineering and Electronics, 125009 Moscow, Russia
* Correspondence: ludmila@sunclass.ire.rssi.ru

**Abstract:** The study presents the results of interferometric processing and analysis of ALOS-1/2 and Sentinel-1 SAR data acquired over the landslide territory of the Bureya river bank in 2006–2018. The novelty of the study is that, for the first time, the joint analysis of interferometric measurements of the landslide movement with meteorological information and time series of SRTM-X, ALOS-1, and TanDEM-X digital elevation models were performed. The results allowed us to make a conclusion that the Bureya landslide was evolving within the frame of the depression formed by a relict landslide which was stable at least at the beginning of the 21st century. The Bureya reservoir filling in 2003–2009 with a 60 m rise of the water and subsequent seasonal water level oscillations supposedly triggered the landslide activity. The landslide movement in the first decade may be characterized by a stable rate of movement all year around. A steady increase in precipitation level in the second decade, with heavy rainfalls in 2013, 2016, and 2018 led to a prominent acceleration of the landslide rate of movement, especially in warm seasons, with a final landslide in December 2018.

**Keywords:** synthetic aperture radar (SAR); differential SAR interferometry; digital elevation model (DEM); landslide; TanDEM-X; the Bureya river

check for updates

**Citation:** Zakharov, A.; Zakharova, L. The Bureya Landslide Recent Evolution According to Spaceborne SAR Interferometry Data. *Remote Sens.* **2022**, *14*, 5218. https://doi.org/10.3390/rs14205218

Academic Editor: Nicola Casagli

Received: 30 August 2022
Accepted: 14 October 2022
Published: 18 October 2022

**Publisher's Note:** MDPI stays neutral with regard to jurisdictional claims in published maps and institutional affiliations.

**Copyright:** © 2022 by the authors. Licensee MDPI, Basel, Switzerland. This article is an open access article distributed under the terms and conditions of the Creative Commons Attribution (CC BY) license (https://creativecommons.org/licenses/by/4.0/).

## 1. Introduction

A giant landslide event on 12 December 2018, on the Bureya riverbank 80 km downstream from the Chekunda settlement, the Russian Far East (50.556°N, 131.476°E), attracted widespread attention because of the catastrophic volume of rocks rushed into the river. It happened in an inhabited hard-to-reach area; so far, the landslide was discovered unexpectedly two days after the event by local hunters riding on the river ice. Two weeks later, the staff of the Khabarovsk Department of the Ministry of Emergency Situations carried out a helicopter survey of the landslide area and confirmed the fact that the rock masses blocked the river. In mid-January 2019, a joint team of people from the Khabarovsk regional government, the Ministry of Emergency Situations, and the Far East branch of the Russian academy of sciences conducted field trip estimations of the size of the landslide and its consequences. According to their preliminary estimations, about 25 million cubic meters of rock debris formed a dam 620 m long and 7–40 m high that blocked the river channel [1,2]. As can be seen on the satellite images, the landslide-generated tsunami wave cleared down 300 ha of forests on the opposite riverbank. The 55 m high wave entered the mouth of the Srednii Sandar tributary on the opposite bank and traveled 3.3 km upstream. Judging by the distribution of the broken ice cover of the Bureya river, the tsunami wave propagated 10–12 km upstream and downstream.

Because of the landslide, the river stream was completely blocked, and the subsequent water level rise created a threat of flooding for nearby settlements, as well as damage to the residential and industrial infrastructure of the hydropower plant downstream. On behalf of the head of the Russian Federation, dated 28 December 2018, the Ministry of Defense of the Russian Federation, on 10 January 2019, started the survey of the river channel and preparatory work to remove the spontaneous dam. After a series of explosions carried out

between 22 January and 3 February 2019, a narrow channel was formed, and the water level above the dam was stabilized. Flood waters of the following spring eroded and expanded the channel significantly, eliminating the flood danger in the future. One of the main unresolved issues now is an understanding of the origin and temporal evolution of this catastrophic landslide event.

InSAR processing applications for landslide studies have been known since the end of the 1990s [3,4]. For surface movement detection, the differential interferometric methods (DInSAR) use an auxiliary digital elevation model (DEM) obtained from independent sources or built from an additional interferometric pair [5,6]. At this moment, DEM is a critical component of interferometric processing, so one can improve its results by choosing the most appropriate DEM [7].

One of the drawbacks of interferometric processing is the temporal signal decorrelation. Changes in the scattering properties of the surface can decrease interferometric coherence dramatically, and that results in phase information loss. The presence of vegetation within the scene is an anticipated source of low interferometric coherence (i.e., decorrelation) in the repeat–pass scheme because of the vegetation cycle, wind displacement of tree branches and foliage, and variations in the moisture content. Alpine mountainous zones (i.e., the altitudinal zones located above the tree line up to the upper limit of plant life) show worse coherence than bare rocks but are still sufficient for C-band data interferometric analysis for the landslides monitoring [8]. Densely vegetated areas usually demonstrate lower coherence values in C- and X-band observations, so stable scatterers such as corner reflectors would be useful for surface movement estimation using the SAR interferometry technique [9,10]. Some authors use two or more observations of the same territory in different frequency bands in order to extract more information about the landslide parameters [11–13]. X-band is the most subjected to decorrelation processes, so the shortest time intervals between observations are required in order to preserve coherence and obtain reliable phase information. C-band data also need rather short time intervals, whereas L-band provides satisfactory interferometric results with a time interval of several months [14] and even years [15]. P-band SAR signals with longer wavelengths can penetrate through the vegetation layer; they demonstrate better correlation, and that could be a solution for the monitoring of landslide hazards in forested areas [16].

However, time series techniques may provide sustainable results even in the case of low decorrelation. This group of methods uses dozens of scenes in order to reveal targets with the most stable scattering properties and to exploit their phase for distinguishing motion-associated phase components within the noisy environment. Whilst classical DInSAR repeat–pass methods can estimate landslide motion for a certain time interval, time series methods (e.g., permanent scatterers [17], short baseline set [18], and others) are much more advanced; they can evaluate atmospheric phase screen and identify pure surface dynamics for a long time interval. Point-target methods are very useful for human-made structures monitoring [19], whereas mountainous slopes covered by vegetation (typical landslide-risk areas) need methods that focus on distributed scatterers (DS). Multi-looking processing is the simplest way to find stable distributed scatterers in the absence of stable point targets at the cost of resolution loss. Among the methods that use DS there are short baseline set (SBAS) [18], SqueeSAR [20], joint-scatterer InSAR (JS-InSAR) [21], temporarily coherent point (TCP-InSAR) [22], and others [23–25]. In some cases, one can combine distributed and point scatterers in one processing chain [25,26]. If seasonal conditions affect the surface displacement pattern over the year significantly, the time series methods can help distinguish periodical and linear parts of the phase trend [27]. One can find a detailed review of the time series methods in [28].

One of the useful applications of the abovementioned methods is the mapping of the landslides both in relatively isolated areas [29,30] and on a country-wide scale [31]. Numerous papers are devoted to the study of landslide evolution, landslide susceptibility, and triggering effects [32–38]. As a rule, the study areas considered are the areas with moderate vegetation. The specificity of our study is determined by the presence of dense

forests on the Bureya riverbanks, including the landslide slope that leads to the strong temporal decorrelation and precludes the exploitation of the advanced techniques based on the analysis of statistics of the long time series SAR data.

## 2. Study Area

The Bureya river is one of the most water-rich inflow streams of the Amur river in the Amur region, the Russian Far East. The river valley is stretched along the border of two large tectonic structures, sharply different in formation—the Bureya mid-range granite massif to the south and the Zeya-Bureya depression to the north. In the riverhead, it is a mountain stream with a 3–4 m/s speed of the current. In the middle reach, it crosses spurs of the Bureyinsky and Turana ranges and runs in the narrow canyon-shaped valley, and in the lower course, it runs along the Zeya-Bureya plain. In the vicinity of the landslide, the width of the valley is 1–1.5 km; it is deeply incised into the ancient leveling surface, the edge of the Turana plateau. The valley profile is asymmetric, with a steep left bank and a distinctly flatter right one. The height of mountain peaks on the left bank is about 400 m, and the steepness of coastal slopes reaches 35°. The right bank is a sloping terrace-shaped surface of erosive nature. The entire territory is characterized by the presence of island, intermittent, and perennial permafrost with a thickness of frozen rocks of an order of 10–100 m. An orographic map of the landslide area (marked by an asterisk) with the Bureya water reservoir and surrounding mountain ranges is presented in Figure 1. This is a modified version of the map from https://maps.me/maps/country-rossiyskaya-federaciya/resource, accessed on 16 October 2022.

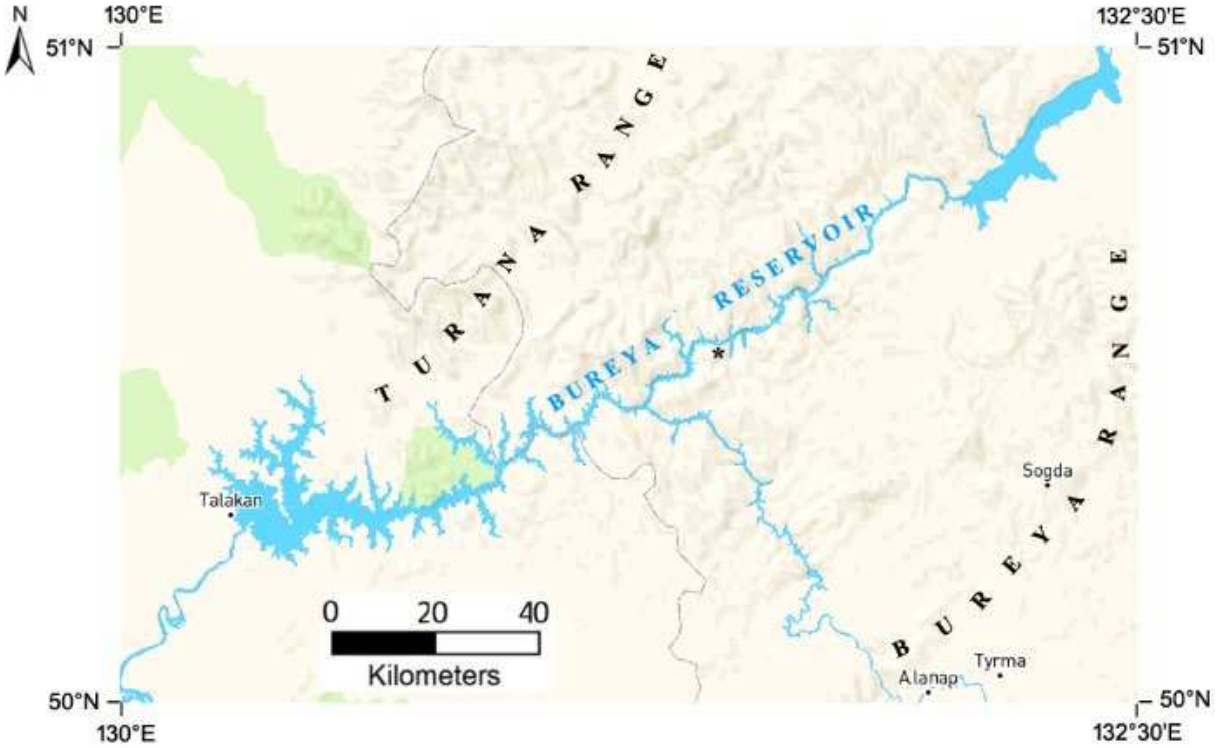


**Figure 1.** Orographic map of the landslide area (marked by an asterisk) with the Bureya water reservoir and surrounding mountain ranges.

According to geological mapping data [39], predominantly intrusive and metamorphic rocks of various ages are distributed in the basin of the middle reach of the Bureya river from the early Proterozoic to the late Paleozoic. The geological description of the territory near the landslide (marked with an asterisk) is presented on the adapted fragment of the geological map (see Figure 2). A relatively narrow strip of a steep valley slope adjacent to the river on the left (southern) bank of the river valley is composed of the Early Proterozoic

rocks represented by solid crystalline schists, biotite schists, amphibolites, biotite, and amphibole injection gneisses. The brown spot to the south is an area of Permian rocks represented by Felsite, quartz-porphyry, lava-breccia, and tuff. The opposite, the right side of the valley, is composed of late Paleozoic leucocratic granites and granite-porphyries [39]. Intrusions of the early-middle Paleozoic geological periods in the upper left and lower right corners of Figure 2 are represented by Biotite and two-mica fine and medium-grained granites. Significant differences in the geological structure of the sides of the Bureya river valley in the vicinity of the landslide allow us to make an assumption about its confinement to the zone of tectonic disturbance.

The climate is sharply continental, with temperatures +28 °C in summer and −25 °C in winter. July is the most pluvious month of the year with 10 rainy days and a monthly rainfall of up to 140 mm. River flash floods are of the monsoon type. Prior to the construction of the Bureyskaya hydropower plant and Bureysky reservoir, floods occurred here almost every year. The water reservoir produces a strong environmental impact, as about 640 km$^2$ of land is flooded, including 465 km$^2$ of forested area.

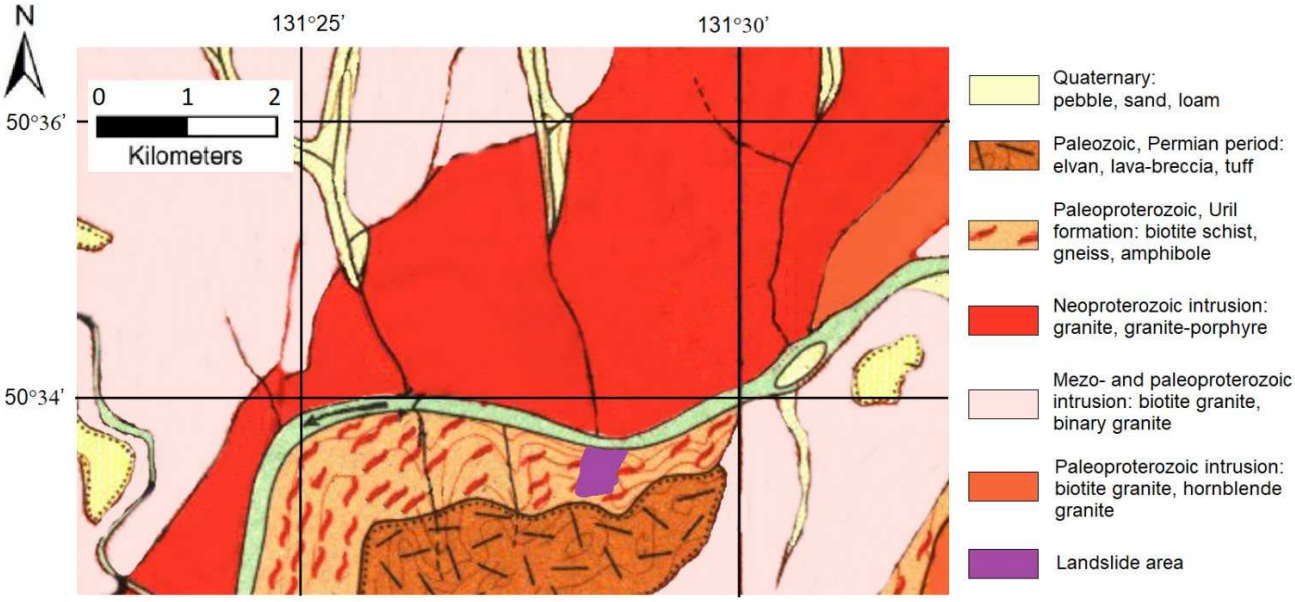


**Figure 2.** Geological description of the territory around the landslide area.

A narrow canyon-shaped riverbed in the vicinity of the landslide area is in the middle of the 230 km long reservoir of the Bureya hydropower plant. The reservoir was filled from 2003–2009. The consequences of the reservoir filling here since April 2003 may be clearly seen on the Google Earth historical images acquired in 2002 and 2006 in the form of the river opening and flooding the watercourses of its tributaries (Figure 3). Because of the rise of the water level, the river width increased here from 200 to 400 m, and the bed of the Srednii Sandar stream, which flows into the Bureya river from the north, was flooded 1.6 km upstream.

According to SRTM-X and TanDEM-X elevation data, the water level at the stream mouth has risen by at least 60 m. Since the river section in the vicinity of the landslide is a part of the reservoir, the seasonal fluctuations of the water level with an amplitude of 16–20 m near the dam also take place here; they cause deforestation in the narrow coastal belt near the water edge (see Figure 4), and very likely they triggered the landslide process. In this picture, taken from a helicopter by A. Makhinov in winter 2019 [40]), arrow 1 marks the forest-free belt near the water edge, 2 marks the landslide circus, and 3 marks slump soils in the river bed.

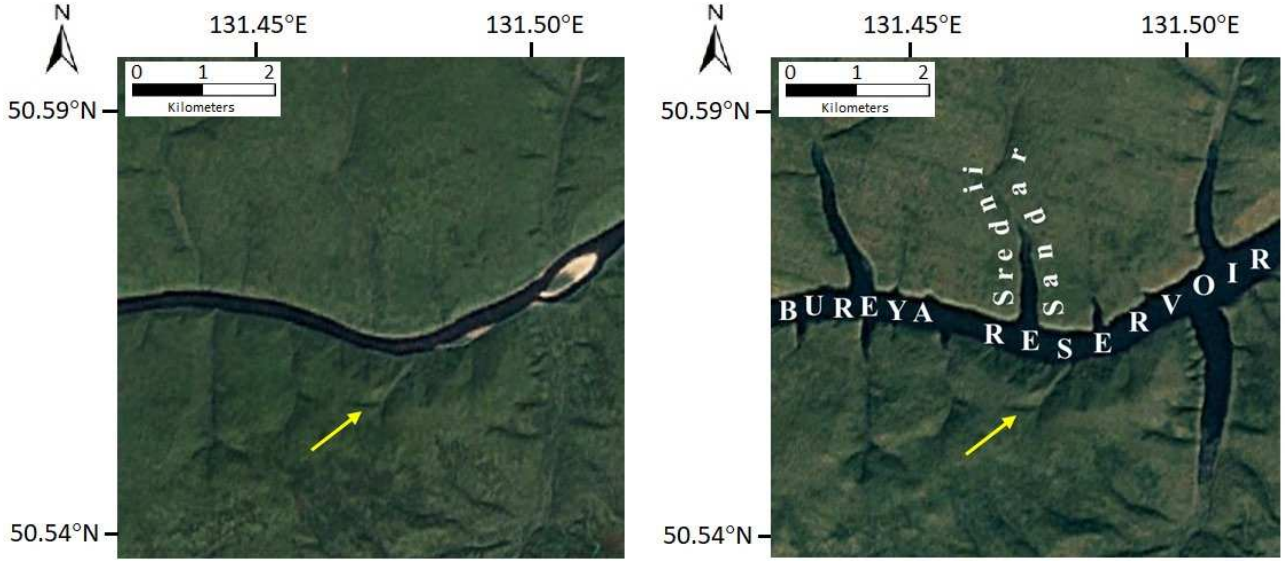


**Figure 3.** Google Earth image of landslide area in 2002 (**a**) и 2006 (**b**) with the landslide area marked by an arrow.

**Figure 4.** Picture of the landslide circus, view from the northeast (arrow 1—forest-free belt; arrow 2—sliding surface; arrow 3—slump debris).

## 3. Spaceborne SAR Data

The efficiency of the repeated orbits interferometry techniques in remote sensing depends heavily on the meteorological conditions and type of underlying covers in the observation area. An essential feature of the landslide area on the Bureya riverbank is the presence of the thick vegetation layer, namely, larch forests. Dense forests, as well as heavy rainfalls in summer, are the reason for the high level of SAR signals temporal decorrelation. Temporal decorrelation is especially high in the short wavelength bands.

Unfortunately, almost all the publicly available archival SAR images covering the Bureya landslide zone, which could be used in our long-term analysis of the development of the landslide process, were acquired in short wavelength bands and, as a rule, with too long time intervals between the repeated observations. For that reason, we did not find promising image pairs in ERS-1/2 data archives (operated 1991–2011), ENVISAT (operated

in 2002–2012), and TerraSAR-X (since 2007), which could have an appropriate temporal coherence. The Sentinel-1 SAR mission is an exception, as archival data available for the study of the Bureya landslide area were acquired every 12 days from 2016 till now.

L-band SAR data (24 cm wavelength) demonstrate higher temporal stability of the backscatter; for that reason, they are preferable for the interferometric measurements on long time intervals. Japanese L-band PALSAR-1 archival images of the Bureya landslide available for analysis covered the period from the summer of 2006, when the reservoir was still not filled up to the design level, till March 2011. PALSAR-2 has been conducting SAR observations since the autumn of 2014 till now. ALOS-1 repeat orbit period is 46 days, and ALOS-2 repeat orbit period is 14 days. Because of the orbit drift and infrequent but intense ALOS-1 orbital corrections, the interferometric baseline varied within a 0–20 km tube during the entire SAR mission. The feature of the ALOS-2 mission is precise, frequent corrections of satellite orbit to keep the satellite trace within the 500 m tube.

## 4. Interferometric SAR Data Processing

SAR acquisitions from the ALOS1/2 and the Sentinel-1A satellites were used to generate time series of interferograms describing the history of the Bureya landslide displacements. The quality of the interferometric phase measurements depends on the coherence of the signals scattered by underlying covers. The complex correlation coefficient or coherence $\gamma$ between two complex SAR images $U_1$ and $U_2$ is defined as:

$$\gamma = \frac{E\{U_1 \cdot U_2^*\}}{\sqrt{E\{|U_1|^2\}E\{|U_2|^2\}}}, \quad (1)$$

where $E\{\}$ denotes the expectation value operator over the array of nearby independent image samples used in the estimation. The analytical expression for the phase as a function of the coherence, according to Cramer-Rao lower bound [41], is:

$$\sigma^2(\Delta\varphi) = \frac{1}{2N_L} \cdot \frac{1-\gamma^2}{\gamma^2}, \quad (2)$$

where $N_L$ is the number of independent pixels on the interferogram used to derive the phase and is usually referred to as the *number of looks*. As can be seen, the larger the coherence, the lower the phase dispersion.

The phase difference $\Delta\varphi$ includes the topographic phase $\Delta\varphi_{topo}$, the phase $\Delta\varphi_d$ generated by small-scale displacements of the underlying surface (surface dynamics), atmospheric phase fluctuations $\Delta\varphi_a$ caused by variations of the signal path length in the atmosphere, extra phase component $\Delta\varphi_s$ in snow cover, as well as random phase fluctuations caused by thermal noise $\Delta\varphi_n$, spatial $\Delta\varphi_{spat}$ and temporal decorrelation $\Delta\varphi_{temp}$, and, finally, unknown initial phase $\Delta\varphi_0$:

$$\Delta\varphi = \Delta\varphi_{topo} + \Delta\varphi_d + \Delta\varphi_a + \Delta\varphi_s + \Delta\varphi_{spat} + \Delta\varphi_{temp} + \Delta\varphi_n + \Delta\varphi_0. \quad (3)$$

The noise of spatial and temporal decorrelation and thermal noise affect the interpixel accuracy of the phase measurements. Noise-like components may be suppressed via interferogram spatial filtering. Atmospheric phase variations caused by the spatial irregularities in the refraction index as well as snow component are slow varying spatial patterns; they may be estimated on the nearby knowingly stable test targets and subtracted.

SAR data processing was performed in the ENVI SARscape processing environment. The topographic phase was estimated using SRTM-X data with 30 m surface sampling and subtracted from the interferometric phase on the interferograms [42]. In order to suppress the noises of various natures, the multi-looking procedure was applied with subsequent interferogram filtering by Goldstein filter [43] having adequate spatial window size 5 × 5 pixels. The total phase of a group of corrupting components from (3)—the

atmosphere, snow, and signal initial phase—was estimated at the nearby stable forested areas near the landslide circus border and subtracted from the phase of the landslide signal.

The remaining surface dynamics phase $\Delta\varphi_d$ can be converted to the line-of-sight (LOS) displacements of the scattering surface $\Delta r_d$ as:

$$\Delta r_d = -\frac{\lambda}{4\pi}\Delta\varphi_d. \quad (4)$$

After that, the LOS displacements can be projected along the landslide slope according to the angle between the satellite track and soil sliding direction, the surface slope angle, and the signal incidence angle [44].

### *4.1. Sentinel-1 SAR Data Processing*

First interferometric studies of the Bureya landslide area were carried out using the data of the European Sentinel-1 C-band synthetic aperture radar [45]. The start of the survey of this region with this satellite falls in the summer of 2016. Two data series acquired from tracks 134 and 61 cover the area of interest and can be used for interferometric studies of landslide dynamics. A total of 90 multitemporal interferograms with 12 days interval between SAR observations were generated. Temporal decorrelation of C-band signals is known to be especially high in vegetated areas. Wind-induced perturbation of vegetation covers, as well as variations of scattering covers, humidity, and freeze–thaw processes, lead to the decrease or even loss of coherence. In contrast, freezing of liquid water in soils and vegetation in wintertime increases media scattering stability and improves coherence. In order to compare the values of the coherence in summer and winter seasons, Figure 5 shows the coherence values from 42 interferometric pairs of Sentinel-1B sessions from 9 November 2017, to 16 March 2019, for track 134. The dates of the first and second observations of the image pair are shown along the horizontal axis in Figure 5. Coherence was calculated for three test areas: landslide slope, forest, and the nonforest area nearby.

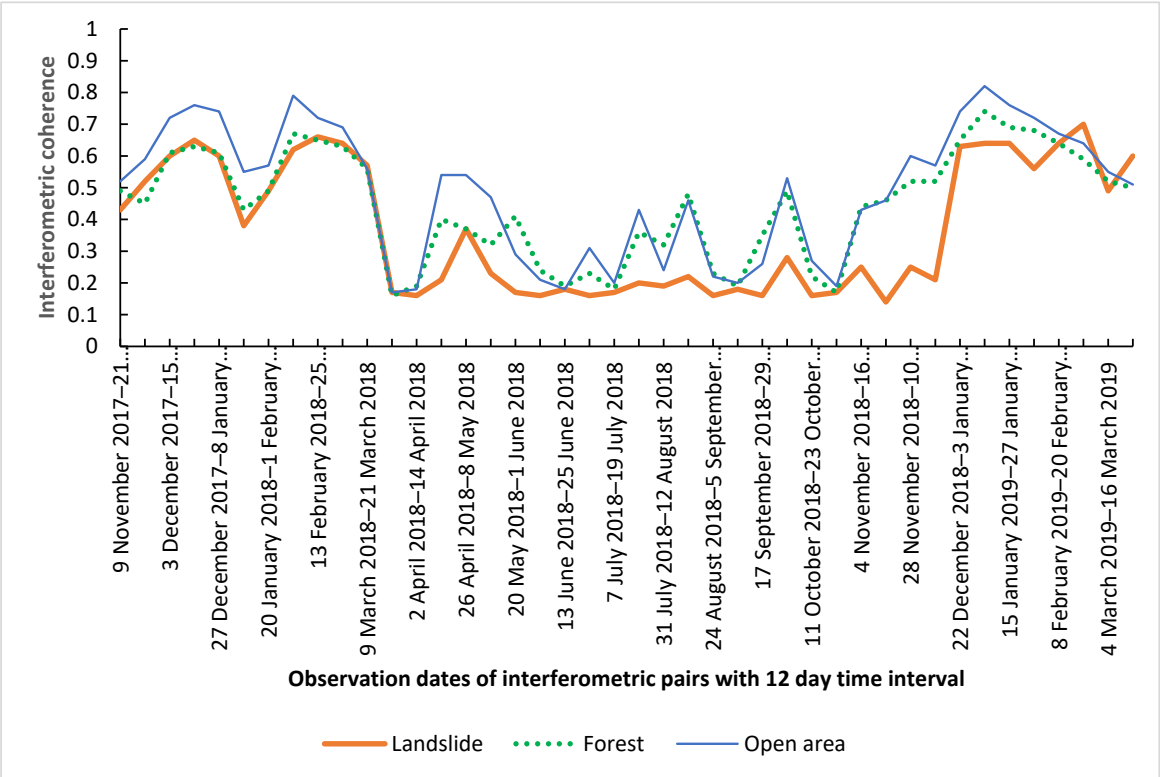


**Figure 5.** Temporal variation of coherence for three areas of interest: open area, forest, and landslide slope.

The coherence of the open area (thin line in Figure 5) is the highest. Forests (dotted line) show generally lower temporal stability. The coherence of the landslide area (solid line) covered with forest should be almost the same as that of the forest test area. That is true for winter 2017–2018 (first quarter of the plot in Figure 5). However, at the end of 2018, the coherence plots of the forest and landslide diverge. Coherence on a landslide slope is low at the beginning of the cold season, in November 2018, in contrast to the coherence of the forested and open areas (right side of the plot in Figure 5). All the coherences are high at the end of December 2018 in the cold weather conditions, a week after the landslide. A probable explanation is that the loss of coherence on the landslide slope at the end of November was caused by a significant acceleration of the landslide in the summer of 2018, with surface displacements larger than the signal wavelength during 12-day observational interval.

Low coherence of the backscatter from these highly vegetated areas in the warm season (middle part of the plot in Figure 5) complicates the monitoring of the landslide even with advanced techniques such as PS or SBAS. The inference on the applicability of PS and PS-like techniques for the monitoring of the Bureya landslide area dynamics can be made relying on results obtained in [46]. Authors of [46] use PSI and SBAS-InSAR methods to assess possible landslide reactivation using multitemporal Sentinel-1B C-band data acquired after the landslide. To exclude corrupting effects of the snow layer on the DInSAR measurements, they selected the SAR data acquired during warm seasons of the years: 3 May–6 October 2019 (14 scenes), 9 May–12 October 2020 (13 scenes), and 4 May–25 September 2021 (12 scenes). As was shown, Sentinel-1 SAR data acquired in warm seasons of the year did not reveal any PS-like points on the Bureya forested banks in the landslide vicinity (see Figure 6). All the PS points detected in their study are located on clear-cut surfaces, including landslide circus and slump soils in the riverbed. In our study, we obtained reliable measurements of the rates of the landslide displacements with accuracy better than 2mm/12 days [47] only in the wintertime of 2016–2017 and 2017–2018 thanks to the high coherence (above 0.5) of the frozen covers backscatter.

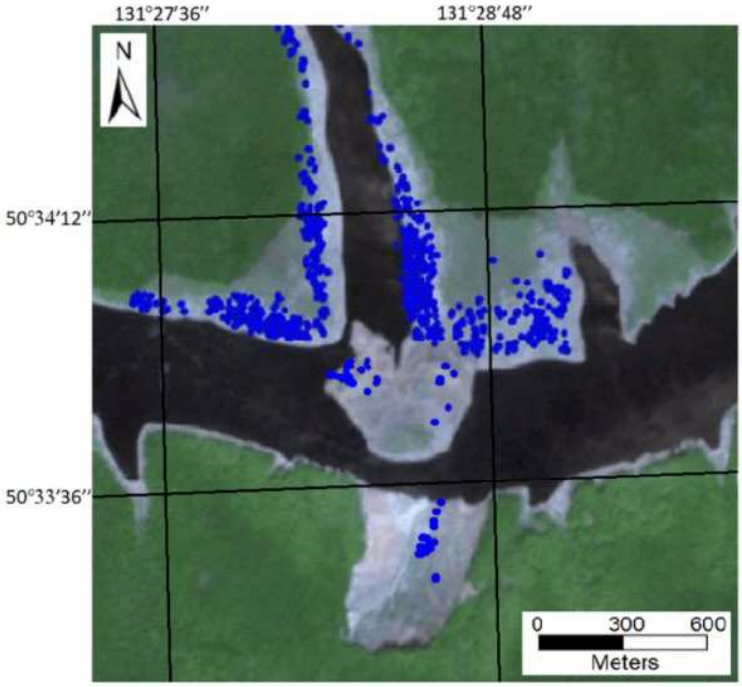


**Figure 6.** Distribution of PS-like points in the landslide area (courtesy of [46]).

Unlike [46], our analysis of the Sentinel-1 SAR data set shows that the landslide circus and surrounding areas seem to have become stable after the landslide, at least in 2019 [48]. We did not observe any displacements with an amplitude of more than 2 mm. However, in two previous winters (2016–2017 and 2017–2018), the interferograms provide clear signs of

surface displacements on the landslide slope [47]. Plots of maximal LOS displacements of the landslide slope in 12-day intervals are in Figure 7.

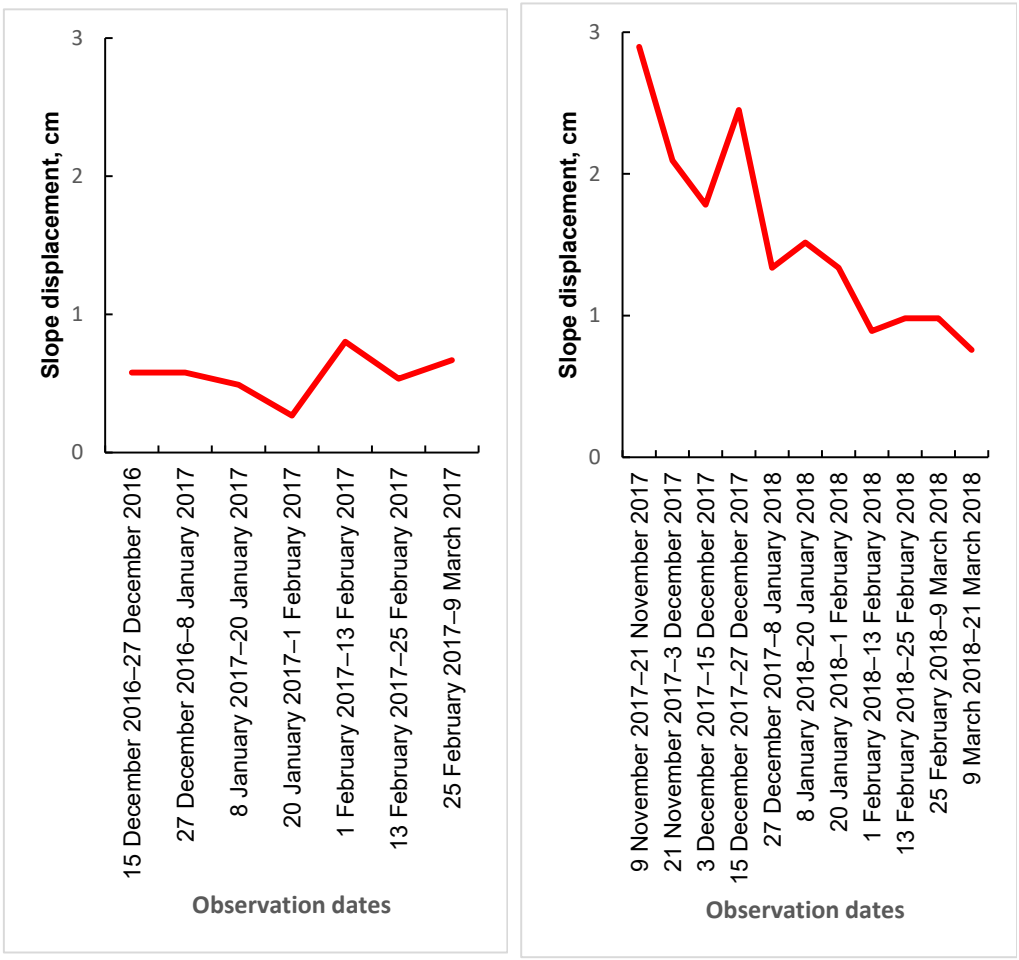


**Figure 7.** Twelve-day displacements of the landslide surface, cm: (**a**) winter 2016–2017; (**b**) winter 2017–2018.

According to the plot in Figure 7a, there was a monotonous 0.7 cm landslip per 12 days in winter 2016–2017. Significantly higher displacement rates were observed at the beginning of the next cold period, 2017–2018 (Figure 7b). It was about 3 cm per 12 days in the beginning, and it decreased to 0.7 cm at the end of the cold period. Taking into account the 32° incidence angle, the 30° slope angle, and the 30° angle between the satellite path and slip direction [44], we can find a correction coefficient of 2.35 to calculate along slope displacements: 7 cm at the beginning and 1.6 cm at the end of the 2017–2018 wintertime.

So far, as a result of the Sentinel-1 data processing, soil slip on the Bureya riverbank could be observed at least since the end of 2016. According to the coherence plots, sharp activation of the landslide activity happened in the summertime of 2018, and it culminated as a large-scale landslide in December 2018.

### *4.2. PALSAR-1/2 SAR Data Processing*

ALOS PALSAR-1/2 L-band SAR data are known to be more applicable for year-round observations of the surface dynamics in the vegetated areas by means of SAR interferometry. However, because of infrequent SAR observations of the territory, there are not too many SAR scenes good for the data stacking and application of persistent scatterer interferometry techniques or similar ones. JAXA archive contains 32 PALSAR-1 images and 16 PALSAR-2 SAR images, applicable for interferometric processing from a formal

point of view. Tables 1–3 contain information about the coherence values of PALSAR-1 interferometric pairs from tracks 414, 415, and 419, with spatial baselines below 4 km and coherence above 0.2. Empty cells mean the coherence here is below 0.2.

**Table 1.** Track 414, ALOS-1 PALSAR coherences.

| Day 1 \ Day 2 | 8 January 2007 | 11 July 2007 | 11 October 2007 | 11 January 2008 | 26 February 2008 | 12 April 2008 | 28 May 2008 | 13 July 2008 | 13 January 2009 | 28 February 2009 | 16 July 2009 | 16 October 2009 | 16 January 2010 | 3 March 2010 | 19 July 2010 | 19 October 2010 |
|---|---|---|---|---|---|---|---|---|---|---|---|---|---|---|---|---|
| 8 January 2007 | | | | | | | | | 0.4 | 0.4 | | | | | | |
| 11 July 2007 | | | 0.2 | | | | | 0.2 | | | | | | | | |
| 11 October 2007 | | | | | | | | | | | | 0.2 | | | | 0.3 |
| 11 January 2008 | | | | | 0.6 | | | | 0.3 | | | | 0.4 | | | |
| 26 February 2008 | | | | | | | | | | | | | | 0.4 | | |
| 12 April 2008 | | | | | | | 0.3 | | | | | | | | | |
| 28 May 2008 | | | | | | | | | | | | | | | | |
| 13 July 2008 | | | | | | | | | | | 0.2 | | | | | |
| 13 January 2009 | | | | | | | | | | | | | | | | |
| 28 February 2009 | | | | | | | | | | | | | 0.4 | | | |
| 16 July 2009 | | | | | | | | | | | | 0.2 | | | 0.2 | |
| 16 October 2009 | | | | | | | | | | | | | | | | |
| 16 January 2010 | | | | | | | | | | | | | | 0.6 | | |
| 3 March 2010 | | | | | | | | | | | | | | | | |
| 19 July 2010 | | | | | | | | | | | | | | | | 0.2 |
| 19 October 2010 | | | | | | | | | | | | | | | | |

Because of the longer wavelength, the PALSAR image pairs may have satisfactory coherence even with 2–3 years between observations. It was also discovered that summer observations of the landslide territory are sometimes less informative because of the strong influence of frequent heavy rainfalls and subsequent temporal decorrelation [49]. Meteorological data from Sektagli station, located 35 km to the west, were used in SAR data analysis (www.rp5.ru, accessed on 16 October 2022) to identify observation dates with heavy rainfall.

Archival images were divided into winter and summer groups, which were processed separately, as strong variations of scattering surface dielectric properties during freezing degraded the coherence.

Interferometric coherence values for 23 PALSAR-1 image pairs over the landslide territory acquired from all three tracks are presented in Figure 8. The largest coherence is typical for the image pairs acquired in cold seasons (diamonds). The coherence decreases expectedly with the lengthening of the period between observations. The coherence of the summer observations made in dry weather conditions is also reasonably high (triangles). Rainfalls during the observation day, or a few days before, with a total amount of rainwater above 40 mm, lead to a dramatic loss of coherence (circles). All the interferometric measurements discussed in the next session below provided a coherence above 0.3.

**Table 2.** PALSAR coherences, track 419.

| Day 1 \ Day 2 | 16 May 2006 | 1 July 2006 | 16 August 2006 | 1 October 2006 |
|---|---|---|---|---|
| 16 May 2006 | | 0.3 | | 0.4 |
| 1 July 2006 | | | | |
| 16 August 2006 | | | | 0.4 |
| 1 October 2006 | | | | |

**Table 3.** PALSAR coherences, track 415.

| Day 1 \ Day 2 | 13 December 2007 | 18 December 2009 | 2 February 2010 | 20 March 2010 |
|---|---|---|---|---|
| 13 December 2007 | | 0.4 | 0.4 | |
| 18 December 2009 | | | 0.6 | 0.4 |
| 2 February 2010 | | | | |
| 20 March 2010 | | | | |

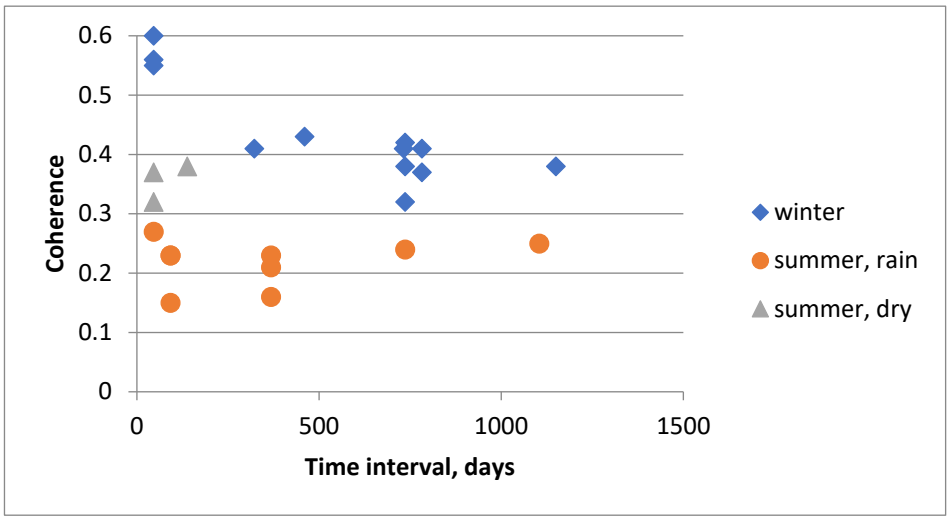


**Figure 8.** ALOS-1 interferometric coherence.

Tables 4 and 5 contain information about the coherence of PALSAR-2 interferometric pairs from tracks 127 and 128. In Figure 9, the interferometric coherence values for 19 PALSAR-2 image pairs over the landslide territory acquired from all two tracks are presented. The largest coherence is typical for the image pairs acquired during cold seasons (diamonds).

**Table 4.** ALOS-2 coherences, track 127.

| Day 1 \ Day 2 | 11 March 2015 | 15 July 2015 | 15 June 2016 | 13 July 2016 | 22 March 2017 | 12 July 2017 | 15 November 2017 | 16 May 2018 | 22 August 2018 | 12 December 2018 | 15 May 2019 |
|---|---|---|---|---|---|---|---|---|---|---|---|
| 11 March 2015 | | | | | 0.3 | | 0.2 | | | | |
| 15 July 2015 | | | | 0.4 | | 0.2 | | | | | |
| 15 June 2016 | | | | 0.5 | | | | 0.2 | | | |
| 13 July 2016 | | | | | | 0.2 | | | | | |
| 22 March 2017 | | | | | | | 0.3 | | | | |
| 12 July 2017 | | | | | | | | 0.2 | 0.3 | | |
| 15 November 2017 | | | | | | | | | | | |
| 16 May 2018 | | | | | | | | | 0.3 | | |
| 22 August 2018 | | | | | | | | | | | |
| 12 December 2018 | | | | | | | | | | | 0.2 |
| 15 May 2019 | | | | | | | | | | | |

**Table 5.** ALOS-2 coherences, track 128.

| Day 1 \ Day 2 | 10 November 2014 | 22 June 2015 | 20 June 2016 | 7 November 2017 | 19 June 2017 | 23 October 2017 | 30 July 2018 | 22 April 2019 |
|---|---|---|---|---|---|---|---|---|
| 10 November 2014 | | 0.2 | | 0.3 | | | | 0.2 |
| 22 June 2015 | | | 0.4 | | | | | |
| 20 June 2016 | | | | | 0.2 | | | |
| 7 November 2016 | | | | | | 0.2 | | |
| 19 June 2017 | | | | | | | 0.2 | |
| 23 October 2017 | | | | | | | | |
| 30 July 2018 | | | | | | | | |
| 22 April 2019 | | | | | | | | |

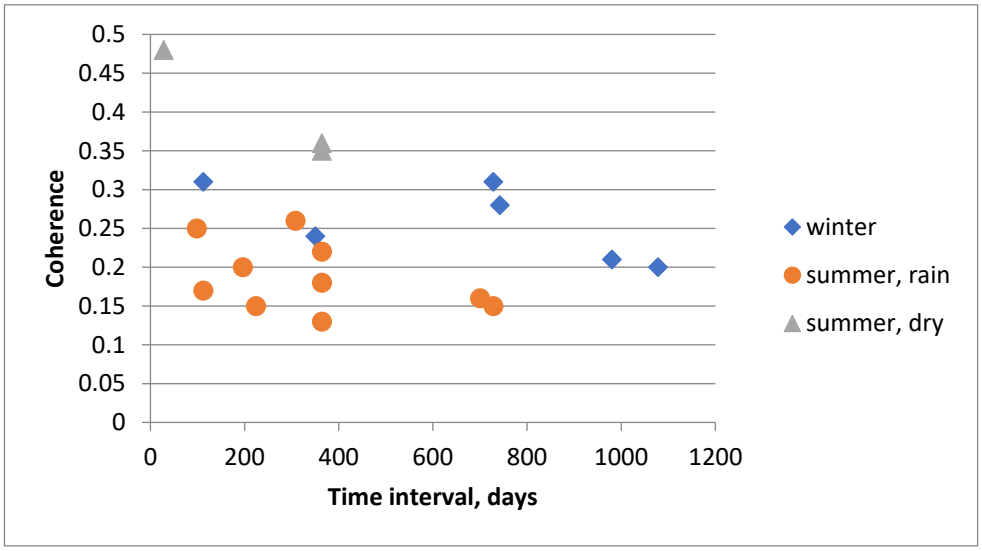


**Figure 9.** ALOS-2 interferometric coherence.

ALOS-2 data pairs have similar coherences and their dependence on the corrupting meteorological conditions. Only 3 summer pairs acquired in the dry weather conditions have comparatively high (above 0.3) coherence among all the 19 data pairs processed. As a result of processing the 42 pairs of ALOS-1 and ALOS-2 images, only 12 interferograms have acceptable coherence on the landslide surface. The displacements measured on PALSAR-1/2 interferograms with subcentimeter accuracy [50] were scaled to a 1-month interval and presented in Figure 10. The triangles mark the displacements at the landslide head and the cubes at the landslide central part.

Analysis of 2006–2010 ALOS-1 measurements (five data points in the left part of the plot in Figure 10) shows that the average velocity of the displacements is approximately the same in relatively short summer 2006 and winter 2009 intervals, as well as in the 2-year long intervals with a very subtle increase in the rate from 2006 to 2010. The velocity was almost the same at the head and in the center of the landslide in 2006–2010. That can be explained by the early and slow stages of the development of the landslide process in 2006–2010. According to ALOS-2 data, velocity increased 2.5 times in 2015–2016 in the 1-year period, covering both summer and wintertime (points 6 and 7). When the measuring period covered only one month in the summer of 2016, the average velocity was 5 times higher (point 8). In addition, the rate of displacements in summertime starting in 2015 in the head is twice higher than in the center. According to PALSAR-1/2 measurements, the

rate of landslide slope displacements rose monotonously by 2017. Moreover, summertime displacements in 2016 and 2017 were twice as high as the average annual ones.

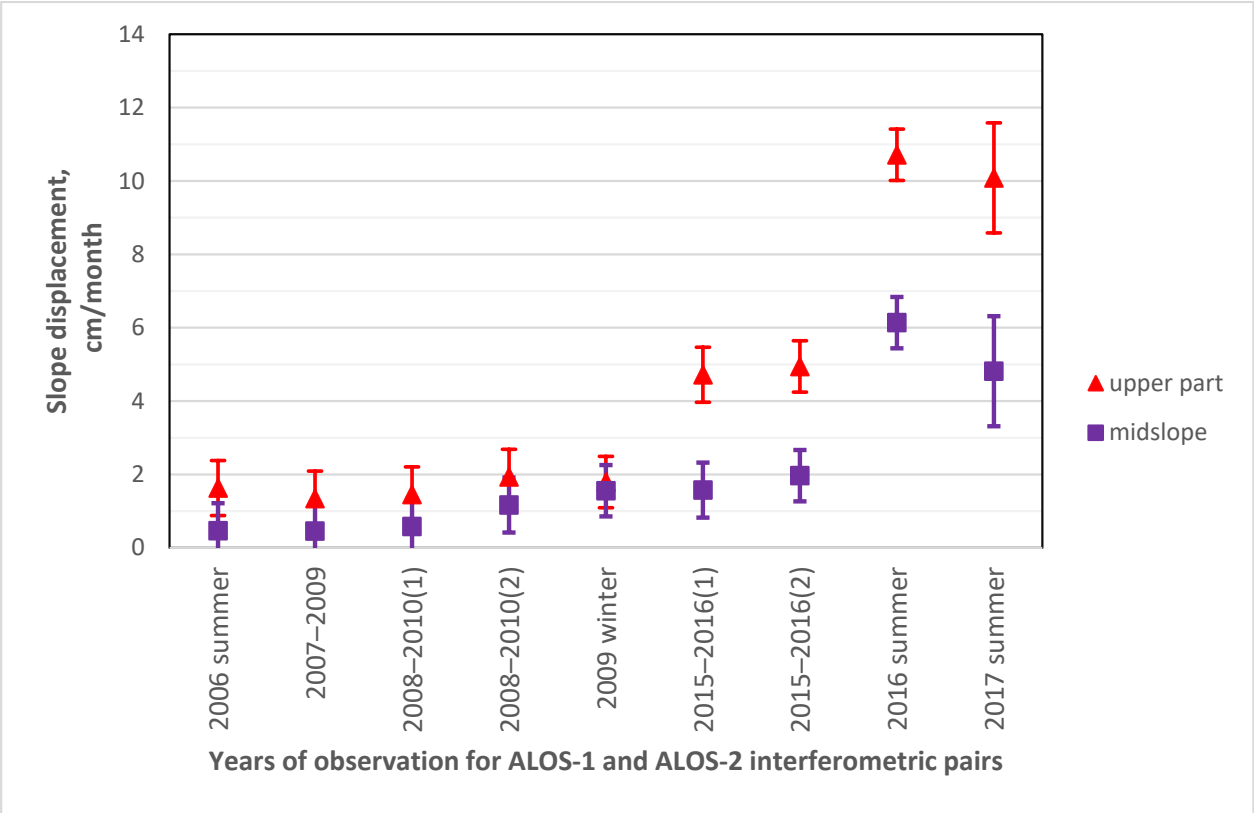


**Figure 10.** Slope displacements along the landslide slope surface derived from PALSAR (2006–2010) and PALSAR-2 (2015–2016) interferograms.

## 5. Processing Results and Discussion

According to the analysis of the rockslides' genesis and their further development, the following triggering mechanisms may be mentioned [51,52]:

- The majority of landslides developing in the hard rocks are reactivated relict landslides;
- Landslides on riverbank slopes usually arise and develop during the first 5–8 years of the reservoir exploitation;
- Significant drawdown of reservoirs (up to 40 m) provides powerful outflows of groundwater from the body of the landslide and leads to the destruction of coastal sandbanks;
- Intense and (or) lasting rainfall or rapid snowmelt can lead to the oversaturation of the slopes and the rise of groundwater levels within the mass, the increase in pore pressure, and reduction in shear resistance;
- Rapid drops in river levels following floods and the rise of groundwater levels result in filling reservoirs, which cause erosion at the base of the coastal slope;
- The development of the landslide process is a function of many factors: the quality of engineering and geological solutions, geological and tectonic structure of coastal massifs, sharp variations in hydrogeological conditions (open filtration of reservoir waters and the formation of groundwater backwater), and water level regime in the reservoir.

The Bureya landslide is very likely a giant reactivated relict landslide. The landslide is located on a very steep (~35°) slope; it extends over a length of 800 m and a width of 400 m. The integration of the phase on the Sentinel-1 29 December 2018–10 January 2019 interferogram within the landslide circus shows that the volume of rocks rushed is about 18.5–18.9 million $m^3$ [45]. According to SRTM and Tandem-X DEMS, this is a combined

rotational–translational landslide. In Figure 11, two plots describing height profiles along the landslide area in 2000 (SRTM DEM) and 2019 (Sentinel-1 29 December 2018–10 January 2019 interferogram) are presented. The horizontal axis is the distance in meters from the landslide head. The profiles cross the middle part of the landslide, and they go from the landslide head to its toe. Maximal depth of the sliding rock layer in the vertical direction is about 100 m.

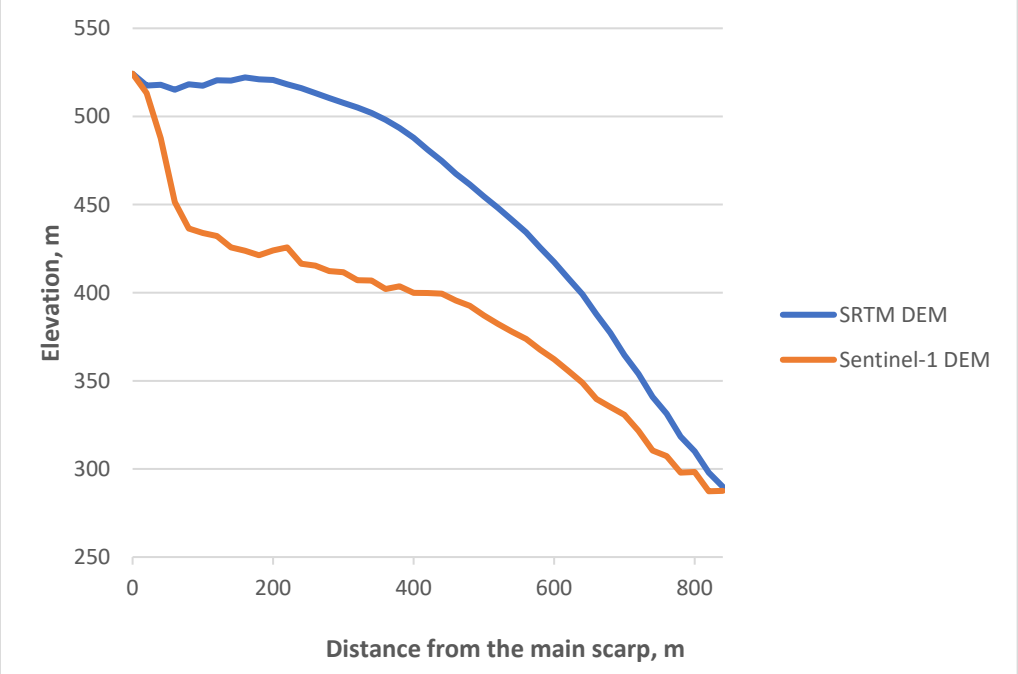


**Figure 11.** Height profiles before (blue line) and after (orange line) the landslide.

A remarkable feature on the SRTM profile at a distance of 50 m is probably the depression or the valley in the head of the landslide. The valley seems to serve as a collector of rain precipitations that moisten the landslide's sliding surface. On the Sentinel-2 optical image, the valley looks like an elongated dark feature in the main scarp area (marked by a red arrow in Figure 12b). The valley is practically unseen on the DEM maps in gray-scale representation because of large-scale variations of the southern bank topography.

Modern high-resolution DEM data from SRTM-X, ALOS-1, and TanDEM-X missions can help improve our understanding of the Bureya landslide history. In Figure 12, left, TanDEM-X shaded DEM of the landslide slope before the landslide is presented. An azimuth of the artificial illumination point here is 245°, and the elevation angle is 50°. Such illumination conditions of the 35° slope of the landslide surface improve the visibility of the landslide surface roughness. Thanks to the exceptionally high surface resolution of TanDEM-X CoSSC DEM data (the acquisition year 2012) being used for the generation of the shadowed relief image, we can see, for the first time there, many topographic features never seen before. In Figure 12c, the Sentinel-2 image, acquired after the landslide, is presented. The walls of the relict landslide depression are clearly highlighted; they look like intermittent black lines in Figure 12a, which underline the location of the main scarp and lateral flanks with a 10–30 m height drop. The red arrow marks the location of the main scarp in the area of the crown, poorly seen on the Sentinel-2 optical image because of the too-low Sun elevation angle in this observation. The rock fall of the year 2018 occurred just within the borders of the topographic depression emphasized in Figure 12a.

(**a**) (**b**) (**c**)

**Figure 12.** Landslide area: (**a**) TanDEM-X shaded DEM; (**b**) Optical Google Earth image before the event; (**c**) Optical Google Earth image after the event. Arrows mark the main scarp location.

The time series of DEMs acquired in SRTM-X, ALOS-1, and TanDEM-X missions (see Figure 13) can shed light, to some extent, on the timeframe of this depression formation. SRTM-X DEM from interferometric SRTM mission (DEM fragment in Figure 13a) was acquired in the year 2000; it is available with a 30 m surface resolution. World 3D DEM data from the ALOS-1 mission (Figure 13b) were collected by PRISM stereoscopic instrument in 2006–2009; they are also available with 30 m resolution. TanDEM-X GDEM data with a similar resolution are in Figure 13c. For better visibility of subtle topography variations in the landslide head, all the maps are given modulo 256 m in elevation. The depression border pointed at with a white arrow, is clearly seen in all the images. Obviously, there was the depression as a footprint of the relict landslide in the year 2000, long before the start of the reservoir filling. In addition, among other morphological features confirming the presence of the relict landslide are an increased roughness of the slope surface within the depression, the presence of the wet (likely) valley on the terrace near the main scarp, and erosive smoothness of the terrace edges. The latter may explain the fact that depression was never identified visually before.

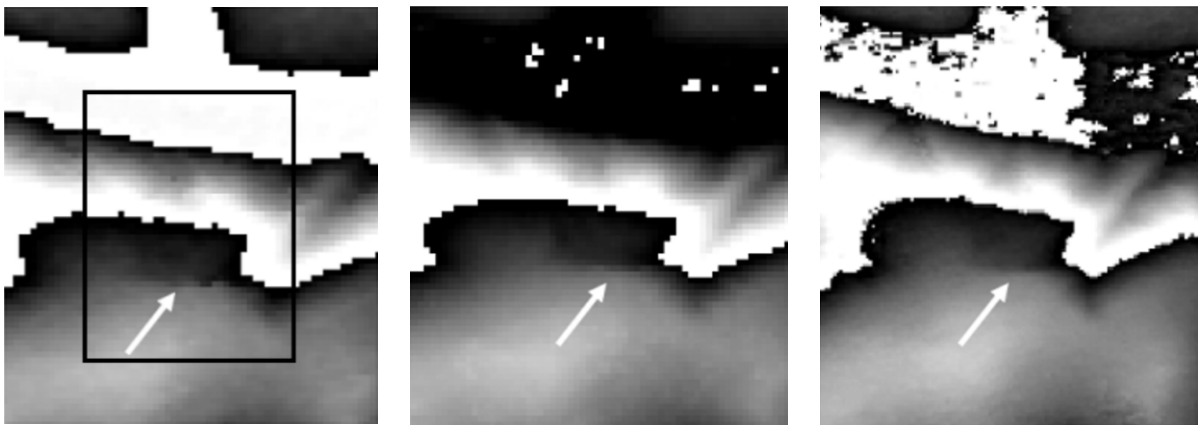

(**a**) (**b**) (**c**)

**Figure 13.** Fragments of DEM for the landslide area: (**a**) SRTM (black rectangle marks the borders of images from Figure 12); (**b**) World3D DEM; (**c**) TanDEM-X. Arrows mark the main scarp. The framework shows the location of the image fragments from Figure 12.

A high integral level of precipitation is considered to be one of the most important triggering factors, along with the moisture ingress into the landslide body from the wetland on the upper terrace and suffosion processes at the base of the landslide caused by annual fluctuations on the water level in the river. There is an obvious correlation between plots

of the annual precipitation level in Figure 14 and the landslide movements in Figure 10. All the average monthly movements observed in the second decade on the PALSAR-2 interferograms are ~3 times larger than those on PALSAR interferograms from the first one. Annual precipitation in the second decade is ~1.3 times larger on average than in the first decade, and the numbers for the year 2016 are almost twice higher. Such a correlation of yearly precipitations with surface deformation rates allows us to make an assumption that the increased level of precipitations played a decisive role in the development of the landslide dynamics in the second decade.

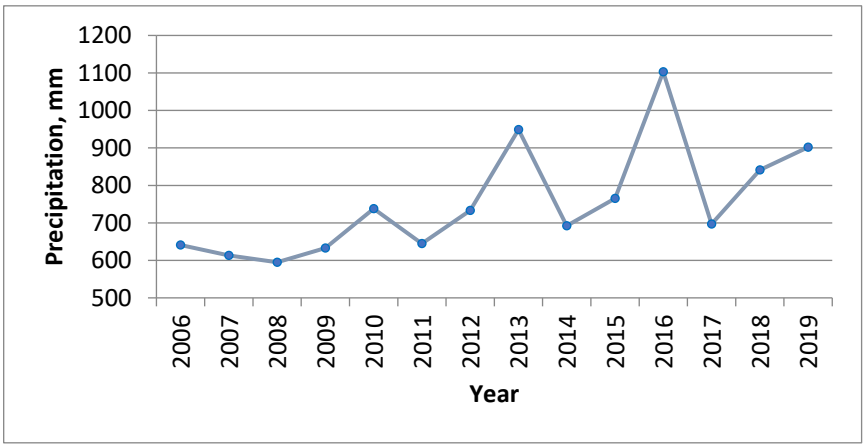


**Figure 14.** Annual precipitation level (in mm) according to Sektagli meteorological data.

A connection between the intra-annual displacement rates and the level of precipitations is illustrated in Figure 15.

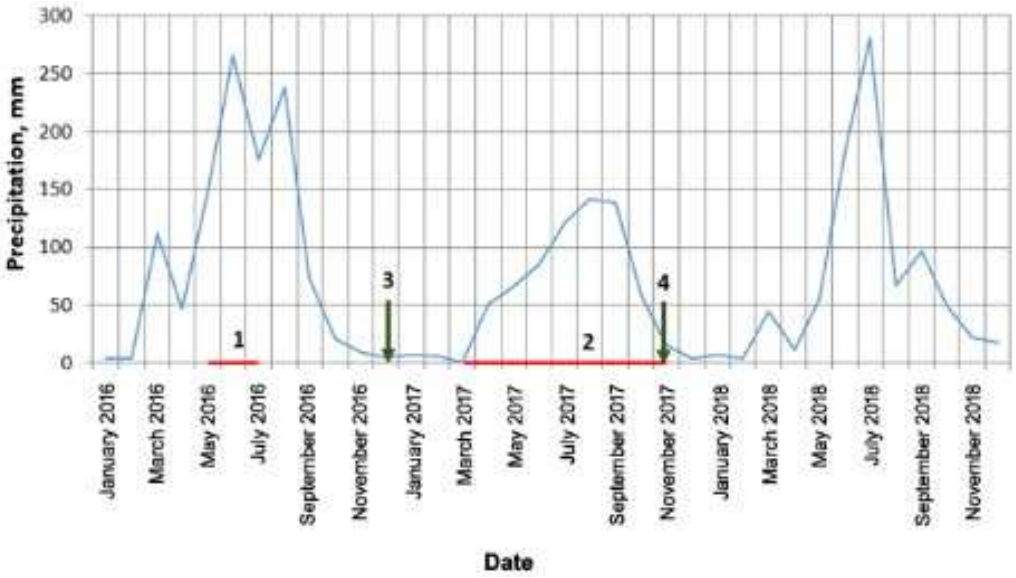


**Figure 15.** Monthly precipitation level (in mm) in 2016–2018 (1—time interval 15 June 2016–13 July 2016, 2—time interval 22 March 2017–15 November 2017, 3 and 4—beginnings of the Sentinel-1 SAR winter observations).

Increased movement rates measured on the interferograms -15 June 2016–13 July 2016 and 22 March 2017–15 November 2017 (last two points in Figure 10) may be explained by the fact that the respective periods between acquisitions of the images, constituting interferometric pairs, explicitly cover summer seasons with intensive rainfalls (red lines with numbers 1 and 2, respectively, in Figure 15). Short rainy interval 1 in the summer of 2016 is an interval between ALOS-2 observations on 15 June 2016 and 13 July 2016.

Additionally, a long and rainy summer interval in the summer of 2017 is an interval between ALOS-2 observations on 22 March 2017 and 15 November 2017.

An arrow number 3 in Figure 15 marks the start of the Sentinel-1 SAR observations in winter 2016–2017 (left plot in Figure 7). An absence of any significant rainfall for about two months before the start of the data collection is probably the reason for the uniform rates of soil movement throughout the winter. At the same time, the following winter measurements started on 9 November 2017, very close to the end of summer rainfalls (arrow number 4 in Figure 15). Water-rich soils that time demonstrate increased velocity here, up to 17 cm per month; the velocity gradually decreased during the next two months to the average typical values of 4–5 cm per month at the end of winter because of the depletion of the excess soil moisture (right plot in Figure 7).

The general picture of the landslide evolution is that in the first decade, the rate of soil movements was approximately the same throughout the year, and in the second decade, it became noticeably higher, especially in summer. The lowest measured rate was noted at the beginning of the interferometric observations in 2006. The likely reasons for the landslide triggering are the filling of the reservoir in 2003–2009 and seasonal fluctuations of water levels because of hydropower plant operation. Growth of the annual precipitation in the second decade, as well as abnormally strong rainfalls in 2013, 2016, and 2018, caused an acceleration of the landslide movement in warm seasons of the year and resulted in the catastrophic landslide finally.

## 6. Conclusions

The presence of the dense forest cover on the Bureya riverbanks restricts the applicability of the radar interferometry techniques significantly. In contrast to the landslide studies in the areas with almost constantly positive temperatures and sparse vegetation, where L-band SAR interferometric studies are applicable all year round [53], and X-band only in summer [54], our results with C-band data were obtained only in the cold season. L-band –data demonstrate high temporal coherence on the long interval, provided the data were acquired in wintertime. In the case of summertime observations, only the short interferometric intervals are admissible. Because of the strong temporal decorrelation of the forests backscatter in the C-band and the unavailability of large time series of L-band SAR data, all the measurements of the landslide movements were made using the classical D-INSAR technique when each differential interferogram was analyzed separately. The measurements of the landslide movements obtained using PALSAR-1/2 and Sentinel-1 convincingly demonstrate the presence of the Bureya landslide process and its evolution from 2006–2018. The results obtained confirm the unique potential of radar interferometry in the long-term monitoring of landslide activity in comparison with ground-based field studies conducted in the summer of 2019 [55], which suggested that the active phase of the landslide process started only a few days before the slope failure.

As it is known, about 80% of large landslides are reactivated on the territory of the relict landslides. The steepness of slopes is an important factor for landslide activation, but slope saturation with water is a primary cause of landslide triggering. The triggering effect may have the form of intense rainfall, snowmelt, changes in the groundwater levels, variations of water level along coastlines, earth dams, reservoirs, canals and rivers, permafrost thawing in the landslide body, etc. The novelty of this study is the conclusion that the Bureya landslide was very likely evolving as reactivated relict landslide, which was stable up to the beginning of the 21st century. The reservoir filling in 2003–2009 with a 60 m rise of the water level and subsequent seasonal water level oscillations triggered the landslide activity. The landslide movement in the first decade was characterized by a stable rate all year around. The steady increase in annual precipitation level in the second decade, with heavy rainfalls in 2013, 2016, and 2018 led to a prominent acceleration of the landslide movement, especially in warm seasons, with final slope failure in December 2018.

**Author Contributions:** Conceptualization, A.Z.; methodology, A.Z. and L.Z.; writing—original draft preparation A.Z., and L.Z.; writing—review and editing, A.Z. and L.Z.; data processing, L.Z.; project administration, A.Z.; funding acquisition, A.Z. All authors have read and agreed to the published version of the manuscript.

**Funding:** This research was carried out with financial support of the Ministry of Science and Higher Education of the Russian Federation in the framework of the Agreement No. 075-01133-22-00.

**Data Availability Statement:** Not applicable.

**Acknowledgments:** The authors thank JAXA for ALOS-1/2 PALSAR data and World 3D DEM, provided under scientific AO projects, German aerospace center DLR for SRTM-X/TerraSAR-X/TanDEM-X data, the European space agency for Sentinel-1/2 data.

**Conflicts of Interest:** The authors declare no conflict of interest.

## References

1. Kramareva, L.S.; Loupian, E.A.; Amelchenko, Y.A.; Burtsev, M.A.; Krasheninnikova, Y.S.; Sukhanova, V.V.; Shamilova, Y.A. Observation of the hill collapse zone near the Bureya River on December 11, 2018. *Curr. Probl. Rem. Sens. Earth Space* **2018**, *15*, 266–271. [CrossRef]
2. Ostroukhov, A.V.; Kim, V.I.; Makhinov, A.N. Estimation of the morphometric parameters of the landslide on the Bureinskoe Reservoir and its consequences on the basis of remote sensing data and field measurements. *Curr. Probl. Rem. Sens. Earth Space* **2019**, *16*, 254–258. [CrossRef]
3. Fruneau, B.; Achache, J.; Delacourt, C. Observation and modelling of the Saint-Étienne-de-Tinée landslide using SAR interferometry. *Tectonophysics* **1996**, *265*, 181–190. [CrossRef]
4. Blonda, P.; Satalino, G.; Alberga, V.; Wasowski, J.; Parise, M.; Chiaradia, M.T.; Viggiano, R.; Pappalepore, M. Soft computing techniques for data classification in a landslide-prone area of Italy. In Proceedings of the IEEE 1999 International Geoscience and Remote Sensing Symposium (IGARSS-1999), Hamburg, Germany, 28 June 1999–2 July 1999. [CrossRef]
5. Nagler, T.; Rott, H.; Kamelger, A. Analysis of landslides in Alpine areas by means of SAR interferometry. In Proceedings of the IEEE 2002 International Geoscience and Remote Sensing Symposium (IGARSS-2002), Toronto, ON, Canada, 24–28 June 2002. [CrossRef]
6. Schiavon, G.; Del Frate, F.; D'Ottavio, D.; Stramondo, S. Landslide identification by SAR interferometry: The Sarno case. In Proceedings of the IEEE 2003 International Geoscience and Remote Sensing Symposium (IGARSS-2003), Toulouse, France, 21–25 July 2003. [CrossRef]
7. Bayer, B.; Schmidt, D.; Simoni, A. The Influence of External Digital Elevation Models on PS-InSAR and SBAS Results: Implications for the Analysis of Deformation Signals Caused by Slow Moving Landslides in the Northern Apennines (Italy). *IEEE Trans. Geosci. Remote Sens.* **2017**, *55*, 2618–2631. [CrossRef]
8. Strozzi, T.; Wegmüller, U.; Werner, C.; Wiesmann, A. Alpine Landslide Periodical Survey. In Proceedings of the IEEE 2002 International Geoscience and Remote Sensing Symposium (IGARSS-2002), Toronto, ON, Canada, 24–28 June 2002. [CrossRef]
9. Xia, Y.; Kaufmann, H.; Guo, X. Differential SAR interferometry using corner reflectors. In Proceedings of the IEEE 2002 International Geoscience and Remote Sensing Symposium (IGARSS-2002), Toronto, ON, Canada, 24–28 June 2002. [CrossRef]
10. Xia, Y. CR-Based SAR-Interferometry for Landslide Monitoring. In Proceedings of the IEEE 2002 In-ternational Geoscience and Remote Sensing Symposium (IGARSS-2008), Boston, MA, USA, 7–11 July 2008. [CrossRef]
11. Lei, L.; Zhou, Y.; Li, J.; Bürgmann, R. Persistent scatterer SAR interferometry application on berkeley hills landslides. In Proceedings of the IEEE 2011 International Geoscience and Remote Sensing Symposium (IGARSS-2011), Vancouver, BC, Canada, 24–29 July 2011. [CrossRef]
12. Di Martire, D.; Confuorto, P.; Frezza, A.; Ramondini, M.; Lòpez, A.V.; Del Rosso, M.P.; Sebastianelli, A.; Ullo, S.L. X- and C-band SAR data to monitoring ground deformations and slow-moving landslides for the 2016 Manta and Portoviejo earthquake (Manabi, Ecuador). In Proceedings of the 2018 IEEE International Conference on Environmental Engineering (EE), Milan, Italy, 12–14 March 2018. [CrossRef]
13. Raucoules, D.; Tomaro, F.; Foumelis, M.; Negulescu, C.; de Michele, M.; Aunay, B. Landslide Observation from ALOS-2/PALSAR-2 Data (Image Correlation Techniques and Sar Interferometry). Application to Salazie Circle Landslides (La Reunion Island). In Proceedings of the 2018 IEEE International Geoscience and Remote Sensing Symposium (IGARSS-2018), Valencia, Spain, 22–27 July 2018. [CrossRef]
14. Asaka, T.; Iwashita, K.; Kudou, K.; Aoyama, S.; Yamamoto, Y. Change detection method for landslide area using RGB color composite image of SRTM and ALOS/PALSAR InSAR DEM: A case study of the Iwate-Miyagi Nairiku Earthquake in 2008. In Proceedings of the IEEE 2011 International Geoscience and Remote Sensing Symposium (IGARSS-2011), Vancouver, BC, Canada, 24–29 July 2011. [CrossRef]
15. Chang, W.; Wang, C.; Chu, C.; Kao, J. Mapping Geo-Hazard by Satellite Radar Interferometry. *Proc. IEEE* **2012**, *100*, 2835–2850. [CrossRef]

16. Xu, Y.; Lu, Z.; Kim, J.-W. P-Band InSAR for Geohazard Detection over Forested Terrains: Preliminary Results. *Remote Sens.* **2021**, *13*, 4575. [CrossRef]
17. Ferretti, A.; Prati, C.; Rocca, F. Permanent scatterers in SAR Interferometry. *IEEE Trans. Geosci. Remote Sens.* **2001**, *39*, 8–20. [CrossRef]
18. Berardino, P.; Fornaro, G.; Lanari, R.; Sansosti, E. Time-Series InSAR Applications Over Urban Areas in China. *IEEE Trans. Geosci. Remote Sens.* **2003**, *40*, 2375–2383. [CrossRef]
19. Perissin, D.; Wang, T. A new algorithm for surface deformation monitoring based on small baseline differential SAR interferograms. *IEEE J. Sel. Top. Appl. Earth Obs. Remote Sens.* **2011**, *4*, 92–100. [CrossRef]
20. Ferretti, A.; Fumagalli, A.; Novali, F.; Prati, C.; Rocca, F.; Rucci, A. A new algorithm for processing interferometric data-stacks: SqueeSAR. *IEEE Trans. Geosci. Remote Sens.* **2011**, *49*, 3460–3470. [CrossRef]
21. Lv, X.; Yazici, B.; Zeghal, M.; Bennett, V.; Abdoun, T. Joint-scatterer processing for time-series InSAR. *IEEE Trans. Geosci. Remote Sens.* **2014**, *52*, 7205–7221. [CrossRef]
22. Zhang, L.; Sun, Q.; Hu, J. Potential of TCPInSAR in Monitoring Linear Infrastructure with a Small Dataset of SAR Images: Application of the Donghai Bridge, China. *Appl. Sci.* **2018**, *8*, 425. [CrossRef]
23. Pepe, A.; Yang, Y.; Manzo, M.; Lanari, R. Improved EMCF-SBAS processing chain based on advanced techniques for the noise-filtering and selection of small baseline multilook DInSAR interferograms. *IEEE Trans. Geosci. Remote Sens.* **2015**, *53*, 4394–4417. [CrossRef]
24. Goel, K.; Adam, N. A distributed scatterer interferometry approach for precision monitoring of known surface deformation phenomena. *IEEE Trans. Geosci. Remote Sens.* **2014**, *52*, 5454–5468. [CrossRef]
25. Fadhillah, M.F.; Achmad, A.R.; Lee, C.-W. Improved Combined Scatterers Interferometry with Optimized Point Scatterers (ICOPS) for Interferometric Synthetic Aperture Radar (InSAR) Time-Series Analysis. *IEEE Trans. Geosci. Remote Sens.* **2022**, *60*, 1–14. [CrossRef]
26. Even, M.; Schulz, K. InSAR deformation analysis with distributed scatterers: A review complemented by new advances. *Remote Sens.* **2018**, *10*, 744. [CrossRef]
27. Shi, X.; Jiang, L.; Jiang, H.; Wang, X.; Xu, J. Geohazards Analysis of the Litang–Batang Section of Sichuan–Tibet Railway Using SAR Interferometry. *IEEE J. Sel. Top. Appl. Earth Obs. Remote Sens.* **2021**, *14*, 11998–12006. [CrossRef]
28. Xue, F.; Lv, X.; Dou, F.; Yun, Y. A Review of Time-Series Interferometric SAR Techniques: A Tutorial for Surface Deformation Analysis. *IEEE Geosci. Remote Sens. Mag.* **2020**, *8*, 22–42. [CrossRef]
29. Kursah, M.B.; Wang, Y. Landslide Inventory Using Insar and Ancillary Datasets for Susceptibility in Western Area, Sierra Leone. In Proceedings of the IEEE 2019 International Geoscience and Remote Sensing Symposium (IGARSS-2019), Yokohama, Japan, 28 July–2 August 2019.
30. Zhao, C.; Liu, X.; Zhang, Q.; Yang, C.; Chen, L. InSAR Application to Baige Landslide Event, China, From Fast Rescue to Catchment Investigation. In Proceedings of the IEEE 2019 International Geoscience and Remote Sensing Symposium (IGARSS-2019), Yokohama, Japan, 28 July–2 August 2019.
31. Ferretti, A.; Novali, F.; Giannico, C.; Uttini, A.; Iannicella, I.; Mizuno, T. A Squeesar Database Over the Entire Japanese Territory. In Proceedings of the IEEE 2019 International Geoscience and Remote Sensing Symposium (IGARSS-2019), Yokohama, Japan, 28 July–2 August 2019. [CrossRef]
32. Reyes-Carmona, C.; Barra, A.; Galve, J.P.; Monserrat, O.; Pérez-Peña, J.V.; Mateos, R.M.; Notti, D.; Ruano, P.; Millares, A.; López-Vinielles, J.; et al. Sentinel-1 DInSAR for Monitoring Active Landslides in Critical Infrastructures: The Case of the Rules Reservoir (Southern Spain). *Remote Sens.* **2020**, *12*, 809. [CrossRef]
33. Barra, A.; Monserrat, O.; Mazzanti, P.; Esposito, C.; Crosetto, M.; Scarascia Mugnozza, G. (2016) First insights on the potential of Sentinel-1 for landslides detection. *Geomat. Nat. Hazards Risk* **2016**, *7*, 1874–1883. [CrossRef]
34. Shano, L.; Raghuvanshi, T.K.; Meten, M. Landslide susceptibility evaluation and hazard zonation techniques—A review. *Geoenviron Disasters* **2020**, *7*, 18. [CrossRef]
35. Polemio, O.; Petrucci, O. Rainfall as a Landslide Triggering Factor: An overview of recent international research. In *Landslides in Research, Theory and Practice, Proceedings of the 8th International Symposium on Landslides, Cardiff, Wales, 26–30 June 2000*; Bromhead, E., Dixon, N., Ibsen, M.-L., Eds.; Thomas Telford: London, UK, 2000; pp. 1219–1226.
36. Irigaray, C.; Lamas, F.; El Hamdouni, R.; Fernández, T.; Chacón, J. The importance of the precipitation and the susceptibility of the slopes for the triggering of landslides along the roads. *Nat. Hazards* **2000**, *21*, 65–81. [CrossRef]
37. Di, B.; Stamatopoulos, C.A.; Stamatopoulos, A.C.; Liu, E.; Balla, L. Proposal, application and partial validation of a simplified expression evaluating the stability of sandy slopes under rainfall conditions. *Geomorphology* **2021**, *395*, 107966. [CrossRef]
38. Take, W.A.; Bolton, M.D.; Wong, P.C.P.; Yeung, F.J. Evaluation of landslide triggering mechanisms in model fill slopes. *Landslides* **2004**, *1*, 173–184. [CrossRef]
39. Vasilieva, V.V. USSR mineral resources map. Scale 1:200 000. Khingano-Bureya series. M-52-XVIII. 1960. Available online: https://www.geokniga.org/maps/7374 (accessed on 16 August 2022).
40. Expedition "Bureya" 2019. Available online: http://tsun.sscc.ru/hiwg/Bureya2019_photos_eng.htm (accessed on 10 August 2022).
41. Rodriguez, E.; Martin, J.M. Theory and design of interferometric synthetic-aperture radars. *Proc. IEEE* **1992**, *139*, 147–159. [CrossRef]
42. Bamler, R.; Hartl, P. Synthetic aperture radar interferometry. *Inverse Probl.* **1998**, *14*, R1–R54. [CrossRef]

43. Goldstein, R.M.; Werner, C.L. Radar interferogram filtering for geophysical applications. *Geophys. Res. Lett.* **1998**, *25*, 4035–4038. [CrossRef]
44. Zakharov, A.I.; Zakharova, L.N.; Krasnogorskii, M.G. Monitoring Landslide Activity by Radar Interferometry Using Trihedral Corner Reflectors. *Izv. Atmos. Ocean. Phys.* **2018**, *54*, 1110–1120. [CrossRef]
45. Zakharova, L.N.; Zakharov, A.I.; Mitnik, L.M. First results of radar monitoring of the landslide consequences on the Bureya riverbank using Sentinel-1 data. *Sovrem. Probl. Distantsionnogo Zondirovaniya Zemli Iz Kosm.* **2019**, *16*, 69–74. [CrossRef]
46. Bondur, V.; Chimitdorzhiev, T.; Dmitriev, A.; Dagurov, P. Fusion of SAR Interferometry and Polarimetry Methods for Landslide Reactivation Study, the Bureya River (Russia) Event Case Study. *Remote Sens.* **2021**, *13*, 5136. [CrossRef]
47. Zakharova, L.N.; Zakharov, A.I. Interferometric Observation of Landslide Area Dynamics on the Bureya River by Means of Sentinel-1 Radar Data in 2017–2018. *Sovrem. Probl. Distantsionnogo Zondirovaniya Zemli Iz Kosm.* **2019**, *16*, 273–277. [CrossRef]
48. Bondur, V.G.; Zakharova, L.N.; Zakharov, A.I. Monitoring the State of the Landslide Zone on the Bureya River in 2018–2019 with Radar and Optical Satellite Images. *Izv. Atmos. Ocean. Phys.* **2020**, *56*, 1520–1527. [CrossRef]
49. Bondur, V.G.; Zakharova, L.N.; Zakharov, A.I.; Chimitdorzhiev, T.N.; Dmitriev, A.V.; Dagurov, P.N. Monitoring Landslide Processes by Means of L-Band Radar Interferometric Observations: Using the Example of the Bureya River Bank Caving. *Izv. Atmos. Ocean. Phys.* **2020**, *56*, 1053–1061. [CrossRef]
50. Bondur, V.G.; Zakharova, L.N.; Zakharov, A.I.; Chimitdorzhiev, T.N.; Dmitriev, A.V. Long-term monitoring of the landslide process on Bureya riverbank based on interferometric L-band radar data. *Sovrem. Probl. Distantsionnogo Zondirovaniya Zemli Iz Kosm.* **2019**, *16*, 113–119. [CrossRef]
51. United States Geological Survey (USGS). The Landslide Handbook—A Guide to Understanding Landslides. 2008. Available online: https://pubs.usgs.gov/circ/1325 (accessed on 16 August 2022).
52. Kondratyeva, L.M. Bureysky landslide and ecological risks. *Vestn. Far East. Branch Russ. Acad. Sci.* **2019**, *2*, 46–55. [CrossRef]
53. Teshebaeva, K.; Roessner, S.; Echtler, H.; Motagh, M.; Wetzel, H.-U.; Molodbekov, B. ALOS/PALSAR InSAR time-series analysis for detecting very slow moving landslides in Southern Kyrgyzstan. *Remote Sens.* **2015**, *7*, 8973–8994. [CrossRef]
54. Motagh, M.; Wetzel, H.U.; Roessner, S.; Kaufmann, H. A TerraSAR-X InSAR study of landslides in southern Kyrgyzstan, Central Asia. *Remote Sens. Lett.* **2013**, *4*, 657–666. [CrossRef]
55. Zerkal, O.V.; Makhinov, A.N.; Kudymov, A.V.; Kharitonov, M.E.; Fomenko, I.K.; Barykina, O.S. Bureya landslide on 11 December 2018. Conditions of the formation and features of the development mechanism. *GeoRisk World* **2019**, *XIII*, 18–30. [CrossRef]